Numerical Calibration of the Mooring System for a Semi-Submersible Floating Wind Turbine Model

Bertozzi, Andrea; Niosi, Francesco; Jiang, Xiaoli; Jiang, Zhiyu

DOI
10.1115/1.4065551

Publication date
2024

Document Version
Final published version

Published in
Journal of Offshore Mechanics and Arctic Engineering

Citation (APA)
Bertozzi, A., Niosi, F., Jiang, X., & Jiang, Z. (2024). Numerical Calibration of the Mooring System for a Semi-Submersible Floating Wind Turbine Model. *Journal of Offshore Mechanics and Arctic Engineering*, *146*(6), Article 062001. https://doi.org/10.1115/1.4065551

ASME Journal of Offshore Mechanics and Arctic Engineering
Online journal at:
https://asmedigitalcollection.asme.org/offshoremechanics

Numerical Calibration of the Mooring System for a Semi-Submersible Floating Wind Turbine Model

Andrea Bertozzi[1]
Maritime and Transport Technology,
Faculty of Mechanical Engineering,
Delft University of Technology,
Delft 2628 CD, The Netherlands
e-mail: a.bertozzi@student.tudelft.nl

Francesco Niosi
MOREnergy Lab, Department of Mechanical
Engineering and Aerospace,
Polytechnic of Turin,
Turin 10129, Italy
e-mail: francesco.niosi@polito.it

Xiaoli Jiang
Maritime and Transport Technology,
Faculty of Mechanical Engineering,
Delft University of Technology,
Delft 2628 CD, The Netherlands
e-mail: x.jiang@tudelft.nl

Zhiyu Jiang
Department of Engineering Sciences,
University of Agder,
Grimstad N-4898, Norway
e-mail: zhiyu.jiang@uia.no

Numerical modeling of the floating offshore wind turbine (FOWT) dynamics plays a critical role at the design stage of a floating wind project. Still, there exist challenges for verification of efficient engineering models against experimental results. Recently, an experimental campaign was carried out for a 1:96 downscaled model of the OC4-DeepCWind semi-submersible platform with mooring lines made of fiber ropes and chains. Leveraging the results of this campaign, this paper focuses on the development and calibration of a numerical model for the semi-submersible platform with a focus on the dynamic responses under bichromatic waves. In the numerical model, the hydrodynamic loads are modeled based on the potential flow theory with Morison drag. The lumped mass method is applied to model the mooring system. Both free decay tests and bichromatic wave conditions are considered in the model calibration process, and key uncertain parameters (e.g., mooring line length) that affect the response have been identified and discussed. Using the proposed calibration procedure, we establish a reasonably good numerical model for prediction of the platform motion and mooring dynamics. The low-frequency responses of the platform under bichromatic waves are well-captured. These outcomes contribute to the development of efficient numerical FOWT models under experimental uncertainty. [DOI: 10.1115/1.4065551]

Keywords: design of offshore structures, floating and moored production systems, fluid-structure interaction, hydrodynamics, ocean energy technology, risers, mooring dynamics, cable dynamics

1 Introduction

The interest for floating offshore wind energy is growing as the world currently faces a pressing need to transition from conventional fossil fuel-based energy sources to sustainable and renewable alternatives. According to the International Renewable Energy Agency, offshore wind power generation will reach approximately 10 TWh by 2050 [1]. Floating offshore wind turbines (FOWTs) are proposed to harness the significant wind energy resource in deep-water environments and to exploit large sea areas distant from the coastline, contributing to increased global renewable energy production [2].

Various design solutions have been proposed for the foundation of such systems, i.e., tension leg platforms, spar buoys, barges, and semi-submersibles. The semi-submersible solution appears to be favorable in the industry because of its versatility with respect to water depth, cost-effectiveness, and simplified transportation and installation processes [3,4]. For design and analysis of any FOWTs, it is crucial to develop accurate, efficient, and reliable engineering tools and associated numerical models. The international community is tackling this challenge by initiating a series of projects to improve modeling methods for offshore wind energy systems. Among the projects, the Offshore Code Comparison, Collaboration, Continued with Correlation (OC5) focuses on the dynamic analysis of the DeepCWind semi-submersible floating wind platform and aims to verify and validate a variety of engineering tools through comparison with experimental data [5]. In OC5, a consistent underestimation is observed of the upwind mooring line tensions in the low frequency (LF) bandwidth when the structure is subject to irregular waves. Robertson et al. [5] attributed this effect to an underestimation of the surge motion of the system at the surge natural frequency.

Following OC5, the sixth phase of the OC project (OC6) focuses on a more detailed investigation on the reasons for the above-mentioned underprediction [6]. New experimental data were collected, in different regular and irregular sea states. In the same framework, Tom et al. [7] selected bichromatic waves to start a new validation campaign between simplified engineering tools and higher-fidelity tools such as computational fluid dynamics (CFD) simulations, to overcome the unfeasibility of simulating irregular wave spectra in CFD environments.

In an experimental or numerical setup, it is interesting to study the behavior of floating platforms under bichromatic waves. The simplest realization of a bichromatic wave is achieved by mixing

[1]Corresponding author.

Contributed by Ocean, Offshore, and Arctic Engineering Division of ASME for publication in the Journal of Offshore Mechanics and Arctic Engineering. Manuscript received November 27, 2023; final manuscript received May 8, 2024; published online June 7, 2024. Assoc. Editor: Amy Robertson.

two monochromatic waves. Wang et al. [8] developed a CFD simulation of a fixed semi-submersible platform invested by frontal bichromatic waves to investigate nonlinear difference-frequency loads to provide a benchmark to validate mid-fidelity tools. Wang and Chen [9] used bichromatic waves to quantify numerical uncertainty of a CFD model of a semi-submersible and apply the results in the validation of the random wave case. However, it is not clear how results from a mid-fidelity engineering tool for the analysis of FOWTs can be directly compared against experimental findings under bichromatic waves.

Recently, Metsch [10] investigated the LF response in the mooring system and the floater motions utilizing a 1:96 Froude scaled model of the OC4-DeepCWind semi-submersible FOWT. During the experimental campaign, decay tests in the moored condition were first executed. The scaled model was also subjected to four different bichromatic waves, obtained by superposing two sinusoidal waves. By choosing appropriate frequencies, the nonlinear LF wave excitation can be studied [7]. During the tests, the wave elevation, platform motions, and mooring line tensions were measured [10]. As indicated in the OC5 and OC6 campaigns, it is a known challenge to establish efficient and accurate numerical models to address the nonlinear platform-surge motion and the upwind mooring line force in the LF bandwidth using a mid-fidelity tool. Niosi et al. [11] showed the importance of calibration when attempting to use models based on linear hydrodynamic theory to predict platform motions.

To address the challenge of uncertain model parameters in numerical calibration, and to understand the influence of key parameters on the prediction of the LF response of the FOWT system under bichromatic waves, this paper develops a hybrid hydrodynamic load model in ORCAFLEX [12]. In this model, large-volume columns and slender pontoons of the floater are modeled by potential flow with Morison drag, and the floater is coupled to the mooring system modeled by the lumped mass method. Then, the developed numerical model is systematically calibrated and compared against the model test results by Metsch and Schreier [13].

Calibration of numerical models of FOWTs against model tests is challenging because of two main reasons. First, as FOWTs are highly coupled dynamical systems, it is practically impossible to tune all influential parameters simultaneously in a numerical model. Second, the aleatoric and epistemic uncertainties are large associated with downscale model tests due to lack of repetitive tests or lack of accurate measurements. In previous numerical calibration works, Rivera-Arreba et al. [2] adjusted the mass and the inertia of a cylinder to match the experimental natural frequency in pitch, and then calibrated the linear-plus-quadratic damping coefficients of the OC5 semi-submersible. Niosi et al. [11] tuned the drag coefficients of the mooring lines of the VolturnUS semi-submersible model. It is essential to develop a numerical model with the same natural frequencies as the physical model to avoid frequency mismatch in the floater motions and mooring line loads. The rigid-body natural frequencies of a floater are influenced by physical properties including the mooring stiffness.

In this work, the fairlead position and the length of the fiber section of the mooring lines are identified as the two most uncertain parameters for tuning of the mooring stiffness. The uncertainties of these parameters are high. Because of the small scale of the model, it is hard to accurately measure fairleads' position, while connections between the different sections of the mooring lines could alter the overall length with respect to the initial design choices.

The rest of the paper is organized as follows. Section 2 outlines the approach for the numerical modeling of an FOWT under wave excitation. Section 3 presents the previous experimental campaign. Section 4 details features of the numerical model. Section 5 presents results of the calibration and discusses the model verification with a focus on the bichromatic wave cases. Finally, Sec. 6 draws the conclusions.

2 Numerical Modeling of FOWTs Subjected to Wave Excitation

2.1 Time-Domain Equation of Motion. The rigid-body dynamics of an FOWT in the presence of nonlinear hydrodynamic loads can be formulated in the time domain. The Cummins' equation [14] is shown in Eq. (1).

$$(\boldsymbol{M}+\boldsymbol{A}_\infty)\cdot\ddot{\boldsymbol{x}}(t)+\int_0^\infty \boldsymbol{B}_r(\tau)\cdot\ddot{\boldsymbol{x}}(t-\tau)\cdot d\tau + \boldsymbol{C}\cdot\boldsymbol{x}(t)=\boldsymbol{F}_{ext} \tag{1}$$

$$\boldsymbol{B}_r(\tau)=\frac{2}{\pi}\int_0^\infty \boldsymbol{B}(\omega)\cos(\omega\tau)\cdot d\omega \tag{2}$$

$$\boldsymbol{A}_\infty=\boldsymbol{A}(\omega)+\frac{1}{\omega}\int_0^\infty \boldsymbol{B}_r(\tau)\sin(\omega t)\cdot d\tau \tag{3}$$

In Eq. (1), $\boldsymbol{M}$ is the mass matrix, $\boldsymbol{A}_\infty$ is the added mass matrix at infinite frequency, the integral term is the retardation function, and $\boldsymbol{C}$ is the hydrostatic stiffness matrix. The state vector $\boldsymbol{x}$ contains the degrees-of-freedom (DOF) of the floater, whilst the right-hand side of the equation, F_{ext} includes all the external forces exerted on the floater, such as the wave excitation loads, viscous drag loads, and mooring forces. Ogilvie [15] derived expressions for $\boldsymbol{A}_\infty$ and $\boldsymbol{B}_r$ based on the hydrodynamic mass and damping matrices determined using radiation–diffraction analysis, as presented in Eqs. (2) and (3), respectively. A numerical integration scheme should be applied to solve Eq. (1) in the time domain.

2.2 Hydrodynamic Loads

2.2.1 First-Order Hydrodynamic Loads. The transfer functions of the hydrodynamic coefficients are computed through the boundary element method based on the potential flow theory. First-order hydrodynamic loads have zero mean value and oscillate with the frequency of the incident wave [16]. They have contribution from radiated, $\boldsymbol{F}_{\boldsymbol{R}}^{(\boldsymbol{I})}$, diffracted, $\boldsymbol{F}_{\boldsymbol{D}}^{(\boldsymbol{I})}$, and incident components, $\boldsymbol{F}_{\boldsymbol{I}}^{(\boldsymbol{I})}$, as given in Eq. (4). The first two components can be computed as in Eq. (5), while the component associated with radiation of waves from the moving body can be calculated through Eq. (6), where ρ is the density; ω is the circular frequency of the wave; n_k is the generalized direction cosine of surface element dS_0 for the k-mode; S_0 is the area of the wet surface immersed in water; ϕ_i, ϕ_d, ϕ_j are the space-dependent terms of the incident, diffracted, and radiated (in the jth direction) wave potentials, respectively; ζ_i, ζ_d, ζ_j, are the harmonic time-dependent terms of the incident, diffracted, and radiated (in the jth direction) wave potentials, respectively; the indices j and k refer to the DOF of the platform [17].

$$\boldsymbol{F}_{\boldsymbol{hydro}}^{(\boldsymbol{I})}=\boldsymbol{F}_{\boldsymbol{R}}^{(\boldsymbol{I})}+\boldsymbol{F}_{\boldsymbol{D}}^{(\boldsymbol{I})}+\boldsymbol{F}_{\boldsymbol{I}}^{(\boldsymbol{I})} \tag{4}$$

$$\begin{aligned}F_{I_k}^{(I)}+F_{D_k}^{(I)}=&-\rho\omega^2\zeta_i e^{-i\omega t}\iint_{S_0}\phi_i n_k\cdot dS_0+\\&-\rho\omega^2\zeta_d e^{-i\omega t}\iint_{S_0}\phi_d n_k\cdot dS_0\end{aligned} \tag{5}$$

$$\begin{aligned}F_{R_k}^{(I)}&=-\rho\omega^2\sum_{j=1}^{6}\zeta_j e^{-i\omega t}\iint_{S_0}\phi_j n_k\cdot dS_0\\&=-\sum_{j=1}^{6}a_{kj}\ddot{x}_j-\sum_{j=1}^{6}b_{kj}\dot{x}_j\end{aligned} \tag{6}$$

2.2.2 Second-Order Hydrodynamic Loads. Second-order loads are proportional to the square of the wave amplitude and have frequencies that are equal to both the difference and the sum of pairs of incident wave frequencies [16]. Second-order wave exciting forces can be described by three important components [17]: mean wave drift load, difference-frequency wave drift load, and sum-frequency wave drift load.

For semi-submersible platforms, the difference-frequency drift loads play a more significant role, because the difference-frequency value can be close to the natural frequencies of the system [16]. Expressions for the second-order LF wave drift forces and moments can be developed using a perturbation method, from direct integration of the pressure obtained from the nonlinear Bernoulli equation on the wet surface. The expressions can then be reformulated in terms of the quadratic transfer functions (QTFs), P^- and Q^-, where $^-$ indicates difference-frequency. P^- and Q^- are transfer functions which give that part of the wave drift force which is in-phase and out-of-phase respectively with the low frequency part of the square of the incident waves [17].

The mean wave drift force results only from nonlinear first-order effects, and can be computed once the first-order potentials are known. The difference-frequency oscillating component includes contribution from the second-order velocity potential. To improve computational efficiency, Newman's approximation [18] was proposed, formulating the extra-diagonal terms of the QTFs, P_{ij}^- and Q_{ij}^-, as in Eq. (7) and in Eq. (8), where P_{ii} and P_{jj} are the diagonal terms of the QTF, computed from the mean drift force, and a_i and a_j are coefficients depending only on the waves frequency.

$$P_{ij}^- = \frac{1}{2} a_i a_j \left(\frac{P_{ii}^-}{a_i^2} + \frac{P_{jj}^-}{a_j^2} \right) \tag{7}$$

$$Q_{ij}^- = 0 \tag{8}$$

For semi-submersible floating platforms, the dynamic response is sensitive to dominant wave frequencies and structural natural frequencies, as large dynamic responses can be excited by the second-order difference-frequency loads. Therefore, only the mean drift force and slowly varying drift force are considered. Previously, Zhang et al. [16] showed that Newman's approximation yields comparable results as the full QTF implementation for prediction of hydrodynamic loads on a semi-submersible FOWT with mooring lines.

2.2.3 Viscous Effects. As PF theory does not account for the viscous loads on the structure, a proper use of semi-empirical method to determine the resultant hydrodynamic force per unit length on cylinders proposed by Morison et al. [19] can be used to solve the problem. The original formulation of Morison's equation for fixed cylinders is as follows:

$$dF_{viscous} = \frac{1}{2} \rho C_D A |u_f - u_s| (u_f - u_s) \tag{9}$$

where $dF_{viscous}$ is the unit length force, ρ is the water density, C_D is the drag coefficient, A is the projected area of a unit length cylinder perpendicular to the flow direction, u_f is the fluid particle velocity component, and u_s is the structure's velocity [16]. The viscous load can be computed by integrating Eq. (9) over the length of a cylinder, and this formula can be adapted to moving structures. For a semi-submersible floater with heave plates and pontoons, Morison's drag is applied to the main columns and the heave plates, whereas the Morison's equation is implemented in its full form (inertia + drag formulation) when treating the slender elements (pontoons).

2.3 Structural Dynamics of Mooring Lines. The mooring lines are treated with a dynamic model based on lumped mass model: the mooring line is discretized into N equal elements connecting N+1 nodes, as illustrated in Fig. 1. All the quantities of interest are computed only at the nodal positions. By applying the equations of dynamic equilibrium to each mass, a set of discrete equations of motion is derived. These equations may be solved in the time domain using finite difference techniques [20]. Moreover, hydrodynamic excitation on the lines is considered by implementing Morison elements (inertia + drag formulation) attached to the line. In addition, the friction between the lines and the seabed is taken into account. The model hence combines internal axial stiffness and damping forces with weight, buoyancy and hydrodynamic forces, and forces from contact with the seabed.

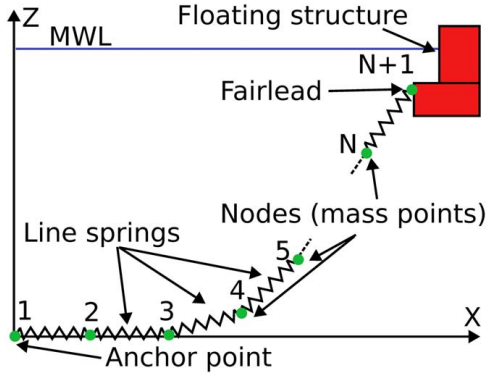

Fig. 1 Discretization of mooring line with a lumped mass method

3 Experimental Campaign of a 1:96 FOWT Model

3.1 General Description. Metsch [10] conducted an experimental campaign utilizing a 1:96 Froude scaled model of a OC4-DeepCWind floater. An overview of the experimental setup is illustrated in Fig. 2, and the scale factors for the main quantities of interest are displayed in Table 1 [21]. When scaling mass, to take into account the density difference between the seawater (ρ_{sw}) and the water in the towing tank (ρ_{fw}), the relation $\gamma = \rho_{sw}/\rho_{fw}$ is used.

Because of the depth limitation of the towing tank and the chosen scale, the mooring system used in the model test is a modification of the original OC5 design [10]. The towing tank has a length of 85 m, a width of 2.75 m, and a depth of 1.25 m. Waves were generated by a hydraulic wave makers operating in piston mode, installed on one of the short sides of the water basin. During the tests, the model was located 28.8 m away from the wave maker. A wave-absorbing

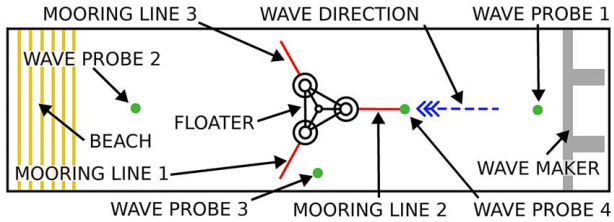

Fig. 2 Overview of the experimental setup

Table 1 List of scale factors for key physical quantities

Variable	Scale factor
Time	$\lambda^{1/2}$
Frequency	$\lambda^{-1/2}$
Length	λ
Mass	$\lambda^3 \cdot \gamma$
Force	λ^3

beach was installed on the opposite end of the tank with respect to the wave maker.

As shown in Fig. 2, four wave gauges placed in different locations in the tank were used to monitor the water elevation in the area. In particular, wave probe 4 is positioned just above the anchor point of mooring line 2. The motions of the floater were measured using a camera system, while the tensions in the mooring lines were monitored through load cells installed between the chain and the fiber section of each mooring line [10].

3.2 Physical Modeling of the Floater With Mooring System. A technical drawing of the floater is shown in Fig. 3 with detailed dimensions of the columns. The pontoons connecting the columns are not present, as this is the computer-aided design (CAD) model used for the panel model.

The mass and inertial properties of the scaled model of the floater were measured again during a second campaign conducted using the same physical model. The measurements collected during the second campaign are utilized in the numerical model and are displayed in Table 2. These data are close to those from Ref. [10]. The position of the center of gravity is given with respect to the global system of reference, located at the mean water level. The

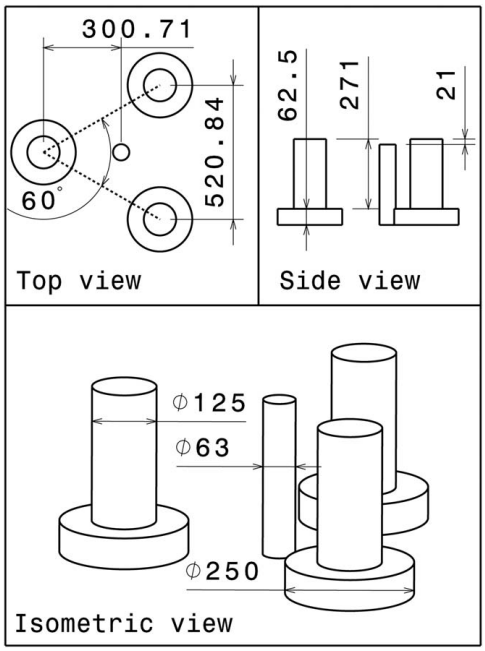

Fig. 3 Geometrical characteristics of the floater (dimensions in millimeters)

Table 2 Inertial characteristics of the scaled model

Center of Gravity (CoG) position	
COG – x coordinate	0 m
COG – y coordinate	0 m
COG – z coordinate	−0.0794 m
Total mass	
Mass	15.9 kg
Inertia tensor (w.r.t. CoG)	
I_{xx}	1.770 kg m^2
I_{yy}	1.788 kg m^2
I_{zz}	1.220 kg m^2

dimensions and orientations of pontoons connecting the columns for the full-scale model can be found in Ref. [22]. The data for the model scale can be found applying a scale factor of 1:96 to the length measurements.

The tower and nacelle were simulated via a 2 m vertical rod installed atop the central columns. These components are made from carbon fiber with added weight. The mass displayed in Table 2 includes this additional weight.

Three mooring lines are used to moor the semi-submersible. The lines used during the investigation are made out of three sections, as illustrated in Fig. 4: from the anchor point, a chain section is followed by an instrumentation section that comprises of a load cell used to measure the tension, and finally, a fiber section connects the line to the fairlead on the floater. The position of the fairlead and the dimensions for the original configuration of the mooring system as presented in Ref. [10] are given in Tables 3 and 4, respectively. Detailed characteristics of the mooring lines are found in Ref. [10].

3.3 Test Program. During the experimental campaign, free decay tests for the moored semi-submersible FOWT were performed first. Then, regular-wave and bichromatic-wave tests were carried out. In total, four different bichromatic wave conditions were investigated.

All the regular waves have an amplitude of 0.02 m with their periods displayed in Table 5. The two regular waves used to build each bichromatic wave and the period of the resultant difference-frequency wave are displayed in Table 6.

Some of the data collected during the experiments are used to calibrate the model, whereas some data are left for validation purposes. In fact, moored decay tests can be used to identify the natural frequency for each DOF; the numerical model can be tuned to reflect the experimental findings. After this calibration, the responses of the numerical model to bichromatic waves are compared to those from the experiment for validation purposes.

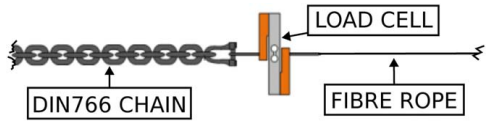

Fig. 4 Illustration of a single mooring line with three sections

Table 3 Estimated positions of the mooring line end points prior to calibration

	x (mm)	y (mm)	z (mm)
End A - to vessel			
ML 2	−426	0	−200
ML 1	213	368.9	−200
ML 3	213	−368.9	−200
End B - to seabed			
ML 2	−1346	0	−1250
ML 1	673	1165.7	−1250
ML 3	673	−1165.7	−1250

Table 4 Uncalibrated lengths of the different sections of each mooring line

ML section	Length (mm)
Fiber rope	629
Load cell	146
DIN 766 chain	1022

Table 5 List of the regular-wave periods

Reg. wave	Period (s)
M1	1.251
M3	1.307
M4	1.369
M5	1.436
M6	1.2

Table 6 Composition and resultant period of bichromatic waves

Bichromatic wave	Regular wave 1	Regular wave 2	Res. Per. (s)
B1	M1	M6	29.2
B3	M3	M6	14.6
B4	M4	M6	9.73
B5	M5	M6	7.3

4 Numerical Modeling and Calibration

4.1 Numerical Analysis. The numerical analysis consists of two stages. At the first stage, frequency-domain analysis is carried out for the panel model using the boundary element method software ORCAWAVE [23]. At the second stage, time-domain analysis is carried out in ORCAFLEX.

4.1.1 Mesh Convergence. To determine a suitable number of panels in the diffraction–radiation analysis, a convergence study is needed. Seven different meshes are considered. The number of panels for each mesh is reported in Table 7. The mean drift loads curves for all meshes and all DOF are compared to each other. The normalized root mean squared error (NRMSE) with respect to the curve generated with the finest mesh (VII) is computed. The goodness of fit is then calculated and used as an indicator of the mesh quality in addition to the NRMSE. A threshold of 0.8 for the goodness of fit is set, as no effect on the motion is observed beyond this threshold. The results of this study for the surge direction is depicted in Fig. 5. Mesh V satisfies the threshold for all DOF. The main features of mesh V are displayed in Table 8.

4.1.2 Frequency-Domain Analysis. The meshed semi-submersible floater is imported into ORCAWAVE to perform diffraction–radiation analysis. The frequency chosen varies from 0.083 Hz to 2.63 Hz to ensure a good exploration of the low-frequency bandwidth. The wave direction varies from 0 deg to 180 deg at an interval of 22.5 deg. The source formulation for solving the potentials is applied and flat panels are used to discretize a curved surface [24,25]. To avoid capturing irregular frequencies associated with the eigenfrequencies of the internal, nonphysical flows of the body, interior surface panels are added [26] to the columns of the semi-submersible.

The pontoons connecting the columns are modeled with Morison elements (Pnt. Mor.), as shown in Fig. 6, with a drag diameter of 0.017 m. To account for the viscous drag, Morison's elements for the vertical columns and central column are implemented with an equivalent diameter of 0.125 m and 0.068 m, respectively. The heave plates at the bottom of the columns are also modeled through Morison elements, with a drag diamater of 0.250 m. The entries for the drag diameters are scaled down by a factor of 96 from the full-scale model [22]. The added mass and drag coefficients are set as in Ref. [22], with drag coefficients in the normal direction to the cylinder's axis set in the order of 0.6 for all elements. To take into account the viscous effects on the vertical direction the axial drag coefficient of the heave plates is set to 4.8.

In ORCAWAVE, the diffraction–radiation problem is reduced to the solution of a linear system, which is solved either through a direct method based on lower–upper decomposition, or through an iterative method based on the modified Gauss–Seidel algorithm [27]. The latter was chosen, after comparing the elapsed time for the diffraction–radiation calculations for the meshes presented in Table 7.

To avoid overestimation of the second-order loads, after the mooring system is implemented in ORCAFLEX, a linear stiffness matrix is retrieved. With an estimation of the external stiffness given by the mooring lines, a new diffraction–radiation calculation is performed, and the results are imported to ORCAFLEX to proceed with the time-domain analysis, followed by calibration and validation of the numerical model.

4.1.3 Time-Domain Analysis. Figure 6 depicts the model implemented in ORCAFLEX. As shown, the global coordinate system is established at the mean water level. After a sensitivity study, the implicit constant time-step for the time integration is set to 0.03 s. The viscous damping of the floater is only represented

Table 7 Meshes used for the convergence study

Mesh identifier	Number of panels
I	1309
II	1925
III	2758
IV	3491
V	4785
VI	6233
VII	10184

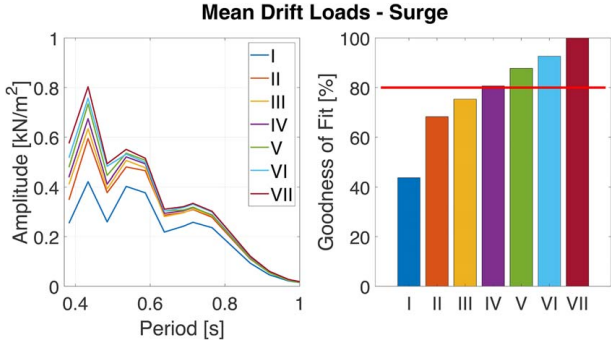

Fig. 5 Results from the convergence study on mean drift loads for the surge direction

Table 8 Mesh V characteristics

Min. panel size	10 mm
Max. panel size	15 mm
Tot. diffraction panels	3152
Tot. panels	4785

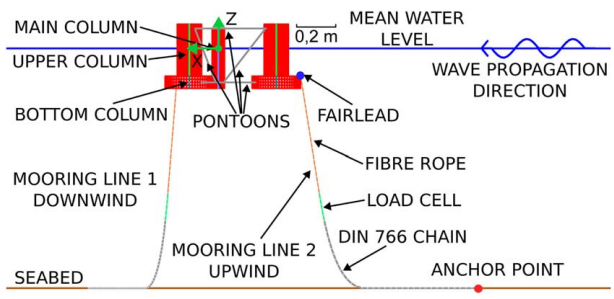

Fig. 6 Overview of the FOWT system

Table 9 Characteristics of the mooring lines

		Fiber rope	Load cell	DIN 766 chain
Outer diameter (mm)		0.67	1.64	9
Mass per unit length (kg/m)		223.9×10^{-6}	0.4384	0.4975
Drag Coefficient. C_D	Nor. (x)	1.2	1.2	2.4
	Ax.	0.08	0.08	1.15
Drag/Lift diameter (mm)	Nor. (x)	—	—	5
	Ax.	—	—	1.59
Added mass coefficient	Nor. (x)	1	1	1
	Ax.	0	0	0.5

by Morison drag. No additional linear or quadratic damping coefficients are implemented.

An equivalent chain approach is used to model the chain segment of each mooring line. The normal added mass coefficient for all the line types and the tangential added mass coefficient for the chain are selected from Ref. [11]. The normal drag coefficient for the chain is set according to Ref. [28]. The mass per unit length of the chain agrees with that reported in Ref. [10].

The load cell is modeled using a simple cylindrical cable element. For the fiber segment of the mooring line, a Dyneema rope with a diameter of 0.67 mm and a mass per unit length of 223.9×10^{-6} kg/m is used. The rope is modeled as a linear elastic material with an axial stiffness of 2.135×10^6 N.

The main properties of the three line types are reported in Table 9. The location of the anchor points, the position of the fairleads, and the lengths of the different sections of each mooring line are listed in Tables 3 and 4, respectively [10].

In the numerical setup, waves are created at the location of wave probe 4 (see Fig. 2), located above the anchor point of the upwind mooring line (ML2). The position of this point is given in Table 10.

4.2 Calibration Procedure. As the focus of this study is on accurate prediction of the surge motion in the low-frequency bandwidth, the calibration procedure must be designed to tune the numerical model such that the platform surge natural period coincides with the one from the experiment which corresponds to 14.6 s [10].

The natural period of an oscillating system is primarily governed by the mass and stiffness of the system. Because of the measurement accuracy, the mass information can be considered to be known, and the calibration of the numerical model should focus on the mooring stiffness. The parameters that affect the mooring stiffness are the position of the fairlead on the floater and the line length.

To limit the computational expense, sequential calibration is proposed. As the measurement uncertainty associated with fairlead position is higher than the uncertainty associated with the length of the fiber section, the fairlead position is first tuned. In this way, the variation of the second parameter, which is more certain, is minimized. The fairlead position is fixed on the value, within the physical constraints, that minimizes the difference between the numerical and experimental value of the surge natural period. Then, the mooring line length is changed by altering the length of the fiber section. The sensitivity analysis allows to determine the value that minimizes the error between the numerical and experimental surge natural period. This procedure is outlined in the flowchart depicted in Fig. 7.

Table 10 Location of wave probe 4

Wave probe 4 position	
X coord	−1.346 m
Y coord	0 m

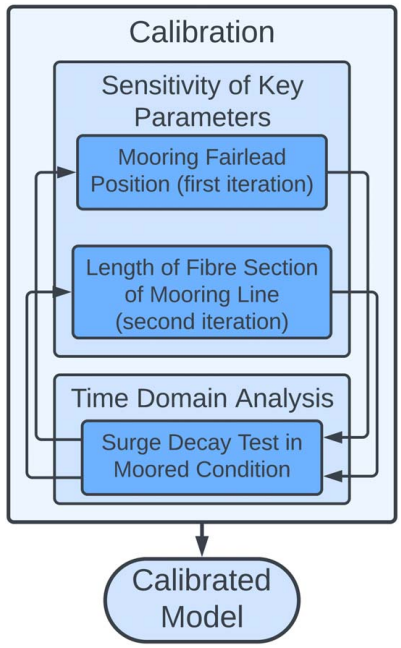

Fig. 7 Calibration procedure

5 Results and Discussion

5.1 Influence of the Model Parameters on the Floater Natural Periods. Once a decay test is executed, the natural period is identified by averaging the time difference between successive peaks of the decay test curve. From the same curve, an approximated value for the non-dimensional damping coefficients can be obtained through the logarithmic decrement approach [29]. When applying this method, the floater-mooring system is approximated by a linearly damped spring-mass system with 1DOF, and the coupling between multiple rigid-body modes, e.g., surge and pitch, is neglected. A first measurement of the numerical natural period for surge resulted in a natural period of 16.5 s.

To align the numerical natural period with the experimental one, the vertical position of the fairlead of each mooring line is tuned first. A sensitivity study is conducted, using seven equally spaced positions ranging from −200 mm to −140 mm. This range was suggested by Metsch [10]. The results for this analysis are depicted in Fig. 8. Even when the line is attached at −140 mm, at the upper edge

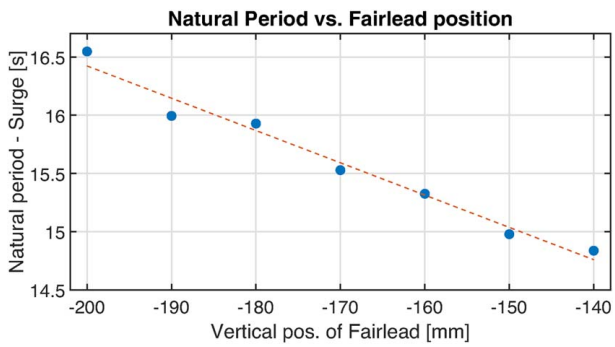

Fig. 8 Results for the sensitivity analysis of the surge natural period versus position of the fairlead

of the heave plate, the numerically obtained natural period is longer than the experimental one. However, moving the fairlead further up would result in a unphysical configuration. For this reason, the length of the fiber section of each mooring line is selected as another parameter to calibrate to further reduce the difference between numerical and experimental results.

A sensitivity study is carried out, varying the length of the fiber segment of each mooring line from 629 mm to 621 mm, with a step of 1 mm. The results for this study are presented in Fig. 9. The sensitivity analysis identifies an optimal fiber segment length of 623 mm. With this length, the relative percentage difference on the natural period for surge is reduced to −0.05% and the difference on the non-dimensional damping coefficient is −3.38%. This value will be further applied in the numerical analysis.

While attempting to adjust the surge natural period, the non-dimensional damping is also measured. There is no significant change in the damping ratio when changing the position of the fairlead, nor when altering the length of the mooring line is observed. The calibrated position of the fairlead and the calibrated length of the mooring line are displayed in Tables 11 and 12, respectively.

Free decay tests for heave, roll, and pitch are executed for the calibrated model. The numerically obtained results together with the experimental ones are listed in Table 13.[2] Although the focus of the calibration is laid on the surge DOF, it is coherent also with the other motions.

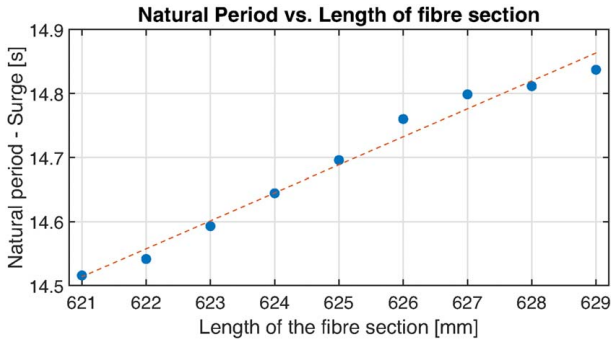

Fig. 9 Results for the sensitivity analysis of the surge natural period versus length of the fiber section

Table 11 Calibrated position of the fairlead (End A)

	End A - to Vessel		
	x (mm)	y (mm)	z (mm)
ML 2	−426	0	−140
ML 1	213	368.9	−140
ML 3	213	−368.9	−140

Note: The position of the anchor point is unaltered.

Table 12 Calibrated lengths of the sections of each mooring line

ML section	Length (mm)
Fiber rope	621
Load cell	146
DIN 766 chain	1022

[2]The experimental data for the pitch decay test were not available.

Table 13 Results for the calibrated decay tests

DOF	Calibrated model (s)	Experimental (s)	Percentual difference (%)
Surge	14.59	14.6	−0.05
Heave	1.80	1.77	1.42
Roll	3.04	2.9	4.67
Pitch	3.05	—	—

5.2 Time-Domain Analysis Under Bichromatic Waves. During the validation phase, the model is subject to five different bichromatic waves whose periods are reported in Table 6.

As no linear or quadratic damping matrices are implemented in the numerical model, over-prediction of the amplitudes of the motions, especially at wave frequencies, are expected to be observed in the validation process. The following results are all presented at model scale.

5.2.1 Wave Elevation. The waves are implemented in ORCAFLEX by superposing the two regular waves considered in Ref. [10], each with an amplitude of 0.02 m. During the experiments, the wave elevation above the anchor of the upwind mooring line is measured by wave probe 4. The simulated water profile accounts for the disturbance of the semi-submersible floater to the wave pattern. The wave elevation is well-captured, as shown in Fig. 10, depicting the wave profile for wave B5. On the other hand, it is important to underline that the small differences observed in Fig. 10 are related to the wave transport phenomena which will have a limited impact on the output and the validation process.

5.2.2 Floater Surge Motion. For each load case, at a first stage, the floater motions in the surge, heave, and pitch are observed and compared with experimental findings.

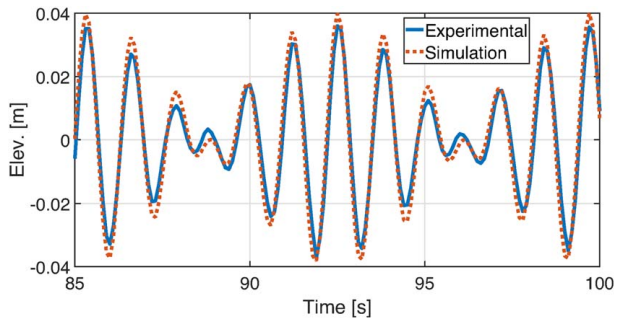

Fig. 10 Water elevation at WP4 under bichromatic wave B5 at model scale

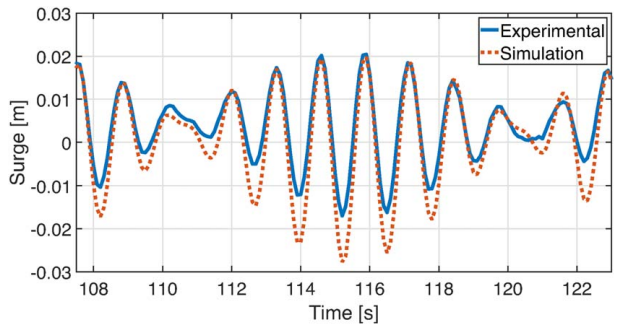

Fig. 11 Platform surge motion under bichromatic wave B4 at model scale

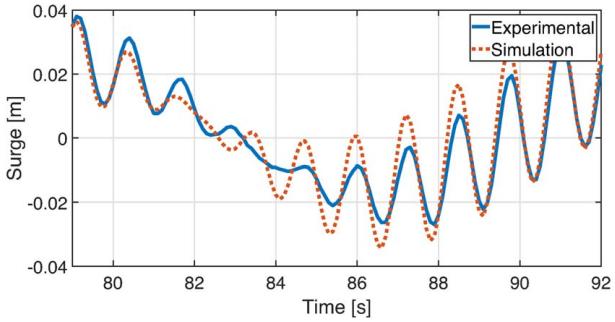

Fig. 12 Platform surge motion under bichromatic wave B3 at model scale

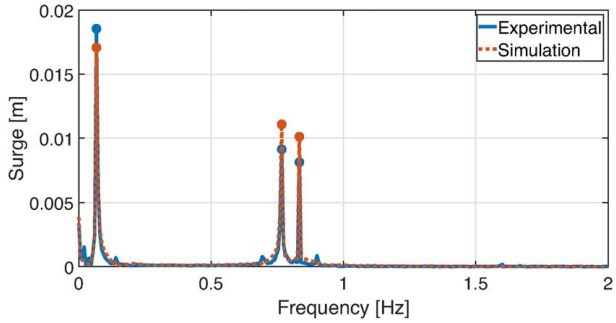

Fig. 14 SSA spectrum of platform surge motion under bichromatic wave B3 at model scale

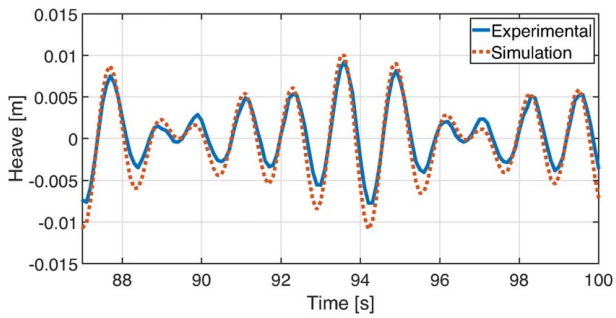

Fig. 15 Platform heave motion under bichromatic wave B5 at model scale

Generally, the maximum amplitudes of surge motions are accurately predicted, as can be observed in Fig. 11 which shows the surge response under the bichromatic wave B4. An over-prediction of the high-frequency oscillation is observed for all load cases, especially in the destructive interference phase. As shown in Fig. 12, the floater surge response under the bichromatic wave B3 has a similar observation.

These observations on the time history results are supported by spectral analysis. All the spectra are obtained through the use of the discrete Fourier transform without any smoothing filters or windows applied. Figure 13 depicts the single-sided amplitude (SSA) spectrum of the surge response to bichromatic wave B1, having a natural period of 29.2 s. Four peaks can be identified. From left to right, the first peak at 0.0342 Hz corresponds to the bichromatic wave B1 frequency, and the peak at 0.0685 Hz corresponds to the resonance frequency of surge. The highest peaks represent the floater's response to the individual components M1 and M6. This observation demonstrates that bichromatic waves are a suitable method to excite the low-frequency response of the moored floater. The over-prediction of the response is more evident at the two higher frequencies, as noted from the time history results.

When analyzing the SSA spectrum for load case B3 depicted in Fig. 14, the response to the individual components M3 and M6 is unchanged with respect to the B1 cases, while in the low-frequency region only one peak is found. This is coherent, as wave the frequency of the bichromatic wave B3, 0.063 Hz, is coincident with the surge natural frequency. In fact, this peak is the highest observed for all load cases.

5.2.3 Floater Heave Motion. When first analyzing the raw data of heave motion, a static offset is noted. This offset is due to a hydrostatic sinkage of the structure. The tracked point in ORCAFLEX initially aligns with the origin of the global coordinate system, located at the mean water level. The position of this point coincides with the computed center of mass of the floater by the CAD model. However, this model does not include the pontoons or mooring lines. For this reason, after adding the weight of the pontoons and connecting the mooring lines to the floater, the floater structure exhibits a static sinkage. Thus, this sinkage must be considered when analyzing the numerical signals.

Figures 15 and 16 depict the time history response and the SSA spectrum of heave under the bichromatic wave B5. The heave motion does not present any low-frequency oscillation. The three peaks captured in the spectrum correspond to the natural frequency of heave at 0.56 Hz and the regular wave periods at 0.69 Hz (M5) and 0.83 Hz (M6), respectively.

5.2.4 Floater Pitch Motion. The model generally overpredicts the amplitude of the oscillations of pitch in the wave-frequency bandwidth. This can be observed in Fig. 17, depicting the pitch response to bichromatic wave B1, and through the SSA spectrum of the response to load case B4, presented in Fig. 18.

In the response spectra for the bichromatic waves B1, B4, and B5, no significant energy in the low-frequency region is observed.

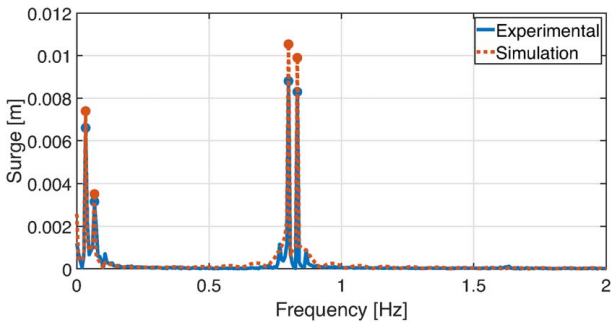

Fig. 13 SSA spectrum of platform surge motion under bichromatic wave B1 at model scale

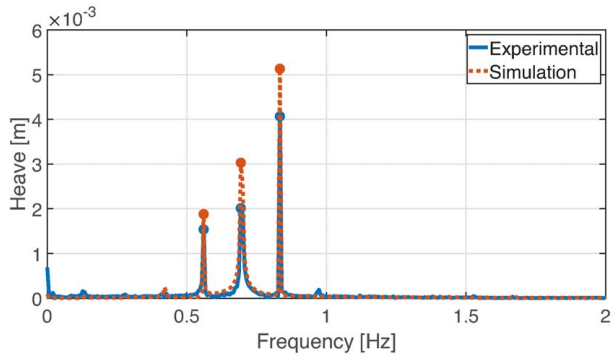

Fig. 16 SSA spectrum of platform heave motion under bichromatic wave B5 at model scale

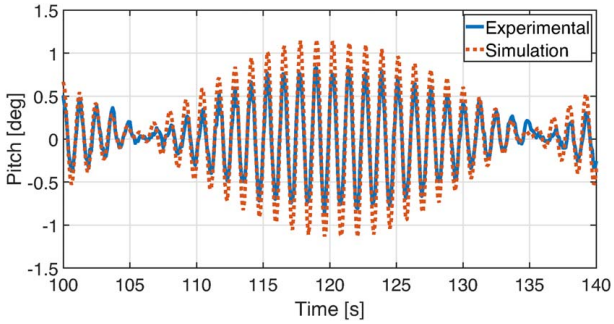

Fig. 17 Platform pitch motion under bichromatic wave B1 at model scale

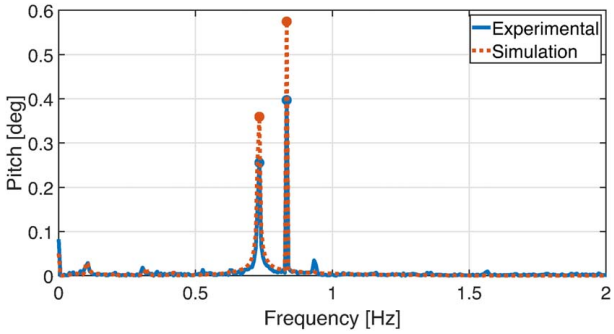

Fig. 18 SSA spectrum of platform pitch motion under bichromatic wave B4 at model scale

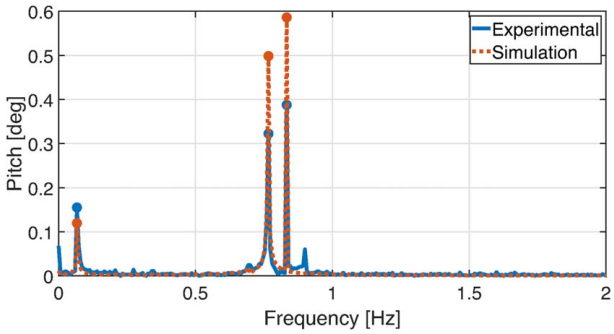

Fig. 19 SSA spectrum of platform pitch motion under bichromatic wave B3 at model scale

When the scaled model is subject to load case B3, which has the same period as the natural period for the surge motion, the coupling between pitch and surge is strong. The floater pitch response displays a low-frequency component at the surge natural frequency, 0.068 Hz, as shown by the spectrum depicted in Fig. 19. The numerical model well predicts the response at this frequency, while the higher frequencies components are still overpredicted.

5.2.5 Mooring Responses. Following the comparison of motion results, mooring line forces are analyzed. The tensions in mooring lines 1 and 2 (ML1 and ML2, respectively) are studied. According to the layout, mooring line 2 is the upwind line, while mooring lines 1 and 3 are the downwind lines. ML1, ML3, and the floater are symmetrical about the *XZ* plane. For this reason, it is sufficient to analyze only mooring lines 1 and 2.

To emphasize the analysis on the dynamics of the force, Metsch takes a static measurement of the pretension of the mooring system and subtracts this value from the time history when analyzing the oscillating response [10]. This procedure is applied to the present numerical results, too.

Table 14 Static forces in mooring lines

	Calibrated model (N)	Experimental (N)	Percentage difference (%)
ML1	1.886	1.50	25.7
ML2	1.884	1.59	18.9

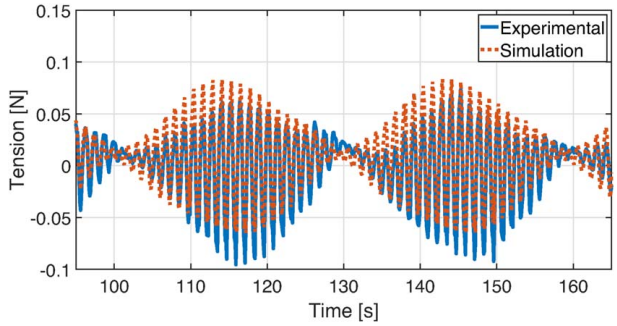

Fig. 20 Tension in ML1 under bichromatic wave B1 at model scale

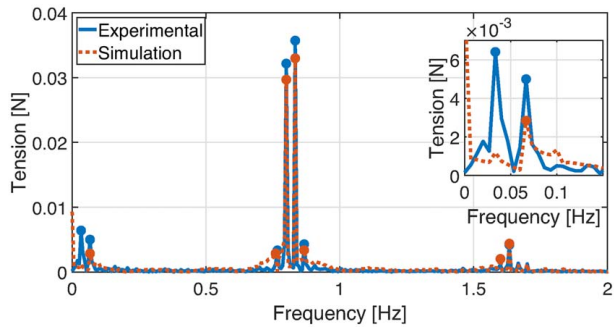

Fig. 21 SSA spectrum of the tension in ML1 for bichromatic wave B1 at model scale

The pretension levels from the experimental setup and from the numerical simulations for ML1 and ML2 are displayed in Table 14. Considering the radial symmetry of the floater and the mooring system, one expects very similar static values for the forces in the three lines. The numerical model validates this hypothesis. It is worth mentioning that Metsch found different values for the mooring forces in the static equilibrium condition between ML1 and ML2 [10].

Figure 20 depicts the time history results for the tension in ML1. The model well replicates the overall behavior observed in experiments. For a better comparison, a frequency-domain study is conducted. The SSA spectrum is presented in Fig. 21. As shown, the numerical model well captures the high-frequency dynamic characteristics of force in ML1. Both frequencies and magnitude in the spectrum are close to those from the experiments. While the experimental response presents components both at 0.0342 Hz (the bichromatic wave B1 frequency) and at 0.0685 Hz (the surge natural frequency), the numerical model only shows surge-frequency response, even though the surge motion spectrum presented both peaks, as shown in Fig. 13. In addition, significant underprediction of the amplitude is observed.

When analyzing the load case B3, we find a good agreement between the numerical and experimental results. The large-amplitude oscillations in the high-frequency bandwidth are accurately captured, as shown in Fig. 22. The amplitude of the low-frequency

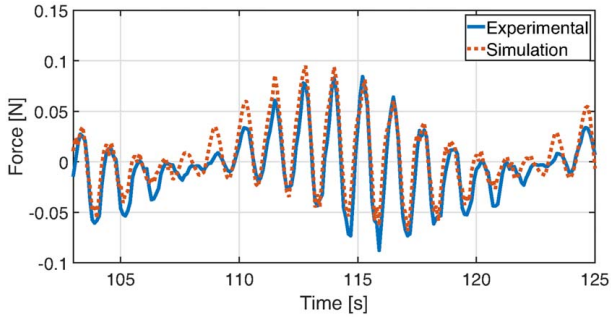

Fig. 22 Tension in ML1 under bichromatic wave B3 at model scale

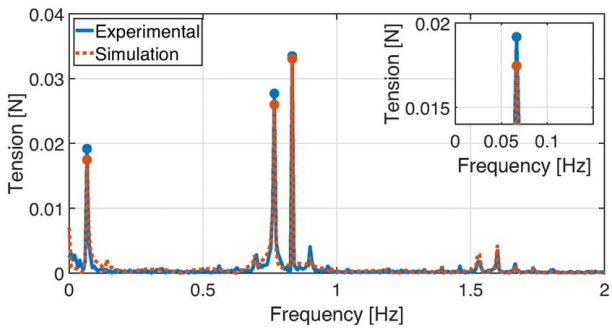

Fig. 23 SSA spectrum of the tension in ML1 under bichromatic wave B3 at model scale

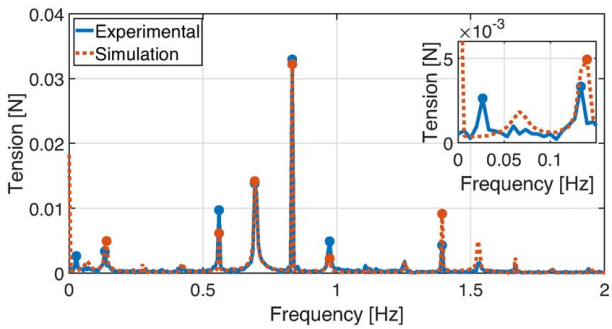

Fig. 24 SSA spectrum of the tension in ML1 under bichromatic wave B5 at model scale

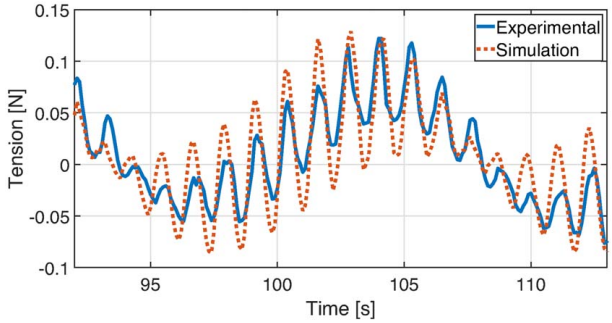

Fig. 25 Tension in ML2 under bichromatic wave B3 at model scale

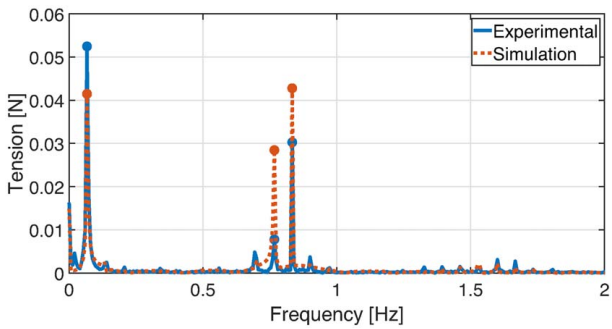

Fig. 26 SSA spectrum of the tension in ML2 under bichromatic wave B3 at model scale

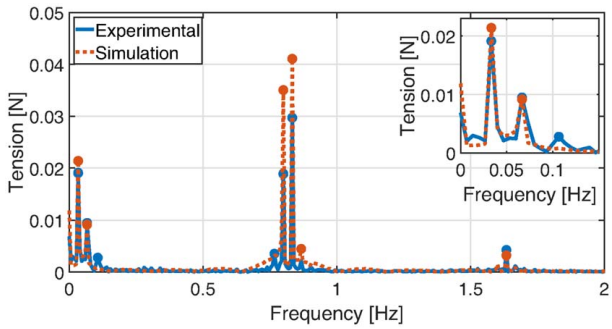

Fig. 27 SSA spectrum of the tension in ML2 under bichromatic wave B1 at model scale

component of the signal is well estimated, as illustrated by the SSA spectrum in Fig. 23.

Similar observations can be found for the bichromatic wave B5. As shown in Fig. 24, the wave-frequency components are well predicted in the SSA spectrum, and the model captures well the bichromatic wave frequency (0.137 Hz) and the heave natural frequency (0.56 Hz). Excitation at higher frequencies is also detected. Such excitation is linked to the natural frequencies of the mooring line and the differences between the numerical and experimental results are large.

Figure 25 depicts a time history for the tension in ML2 when the semi-submersible FOWT is subject to the bichromatic wave B3. This load case provides the largest excitation in the low frequency for the surge, as the wave period is coincident with the surge natural period. High-frequency oscillations are largely overpredicted by the numerical simulation, while the low-frequency variation in the force is more accurately calculated, as reflected by the SSA spectrum shown in Fig. 26. Similar behavior is observed for the mooring tension under the bichromatic wave B1, as depicted in Fig. 27. The low-frequency components at the bichromatic wave frequency (0.034 Hz) and at the surge natural frequency (0.0685 Hz) are both captured. A substantial overestimation of the higher frequency components is observed.

6 Conclusion

In this paper, the development of a numerical model for a semi-submersible floating wind turbine is presented. Mesh convergence studies were performed to ensure accuracy of the diffraction–radiation analysis, and time-step sensitivity was investigated to optimize the time-domain numerical integration. The numerical model is first calibrated against experimental data of moored decay tests to achieve a good match of the floater natural periods. Then, bi-chromatic wave conditions are considered to excite the system in the low-frequency region, and the simulated responses are systematically compared against the experimental ones.

The calibrated numerical model can accurately predict the wave-induced motions of the floating wind turbine in the time domain. The predicted mooring line tensions are relatively less accurate. Despite the deviation in the static pretension of the mooring lines, the trend of variation in the dynamic mooring tension is well-captured. Overall, the calibrated numerical model is deemed satisfactory in predicting the motion and the forces in the low-frequency region under bichromatic waves.

Although fine tuning of fairlead position and mooring line length, as shown in this work, allows a better prediction of the mooring loads frequencies and magnitudes, other parameters could have an impact on the numerical model response. In future work, the discrepancies observed in the magnitude of the mooring tension could be further reduced with more accurate measurements of the floater volume and inertia, and by calibrating other parameters, such as drag coefficients of the floater and of the mooring lines. The execution of experimental free decay test for the floater in the unmoored condition should be considered for an effective calibration of those parameters.

Conflict of Interest

There are no conflicts of interest.

Data Availability Statement

The datasets generated and supporting the findings of this article are obtainable from the corresponding author upon reasonable request.

References

[1] IRENA, 2022, World Energy Transitions Outlook 2022: 1.5 °C Pathway Outlook Report, International Renewable Energy Agency, Abu Dhabi, UAE, http://www.irena.org/publications/2022/Mar/World-Energy-Transitions-Outlook-2022.

[2] Rivera-Arreba, I., Bruinsma, N., Bachynski, E. E., Viré, A., Paulsen, B. T., and Jacobsen, N. G., 2018, "Modeling of a Semisubmersible Floating Wind Platform in Severe Waves," International Conference on Offshore Mechanics and Arctic Engineering, Vol. 51302, American Society of Mechanical Engineers, p. V009T13A002.

[3] Du, A., 2021, Semi-Submersible, Spar and TLP – How to Select Floating Wind Foundation Types? https://www.empireengineering.co.uk/semi-submersible-spar-and-tlp-floating-wind-foundations/ Website of Empire Engineering. Accessed June 15, 2023.

[4] Elisa Romero, C. W., 2023, Floating Wind Logistics and Supply Chain Requirements—The Challenges of Commercialization: https://brightspace.tudelft.nl. Guest Lecture from Heerema Engineering Solutions in the Series AE4W31 Floating Offshore Wind Energy. Accessed June 15, 2023.

[5] Robertson, A. N., Wendt, F., Jonkman, J. M., Popko, W., Dagher, H., Gueydon, S., and Qvist, J., 2017, "OC5 Project Phase II: Validation of Global Loads of the DeepCwind Floating Semisubmersible Wind Turbine," Eng. Proc., **137**, pp. 38–57.

[6] Robertson, A., Gueydon, S., Bachynski-Polić, E., Wang, L., Jonkman, J., Alarcon Fernandez, D., and Amet, E., 2020, "OC6 Phase I: Investigating the Underprediction of Low-Frequency Hydrodynamic Loads and Responses of a Floating Wind Turbine," J. Phys. Conf. Ser, **1618**(Future Wind), p. 032033.

[7] Tom, N., Robertson, A., Jonkman, J., Wendt, F., and Böhm, M., 2019, "Bichromatic Wave Selection for Validation of the Difference-Frequency Transfer Function for the Oc6 Validation Campaign," International Conference on Offshore Mechanics and Arctic Engineering, Vol. 59353, American Society of Mechanical Engineers, p. V001T01A022.

[8] Wang, L., Robertson, A., Jonkman, J., Yu, Y.-H., Koop, A., Borràs Nadal, A., Li, H., Shi, W., Pinguet, R., and Zhou, Y., et al., 2021, "Investigation of Nonlinear Difference-Frequency Wave Excitation on a Semisubmersible Offshore-Wind Platform With Bichromatic-Wave CFD Simulations," International Conference on Offshore Mechanics and Arctic Engineering, Vol. 84768, American Society of Mechanical Engineers, p. V001T01A009.

[9] Wang, Y., and Chen, H.-C., 2023, "Verification and Validation of Computational Fluid Dynamic Simulations of a FOWT Semi-submersible Under Bichromatic and Random Waves," ASME J. Offshore Mech. Arct. Eng., **145**(6), p. 062001.

[10] Metsch, Y., 2023, "Experimental Low Frequency Mooring Analysis of a Floating Offshore Wind Turbine," M.S. thesis, Delft University of Technology, Delft, The Netherlands.

[11] Niosi, F., Dell'Edera, O., Sirigu, M., Ghigo, A., and Bracco, G., 2023, "A Comparison Between Different Numerical Models and Experimental Tests for the Study of Floating Offshore Wind Turbines," The 33rd International Ocean and Polar Engineering Conference, Ottawa, Canada, June 2023.

[12] Orcina, 2023, OrcaFlex Documentation. https://www.orcina.com/webhelp/OrcaFlex/Default.htm. Retrieved on November 19, 2023.

[13] Metsch, Y., and Schreier, S., 2023, "Data Underlying the MSc Thesis: Experimental Low Frequency Mooring Analysis of a Floating Offshore Wind Turbine.

[14] Cummins, W., 1962, "The Impulse Response Function and Ship Motions," Symposium on the Ship Theory, Hamburg, Germany, January 1962.

[15] Ogilvie, T., 1964, *Toward the Understanding and Prediction of Ship Motions*, Technische Hogeschool Delft, Delft, The Netherlands.

[16] Zhang, L., Shi, W., Karimirad, M., Michailides, C., and Jiang, Z., 2020, "Second-Order Hydrodynamic Effects on the Response of Three Semisubmersible Floating Offshore Wind Turbines," Ocean Eng., **207**, p. 107371.

[17] Journée, J. M. J., and Massie, W., 2001, *Offshore Hydromechanics*, 1st ed., Delft University of Technology, Delft, The Netherlands.

[18] Newman, J. N., 2018, Marine Hydrodynamics, 40th Anniversary Edition ed., The MIT Press, Cambridge, MA.

[19] Morison, J., Johnson, J. W., and Schaaf, S. A., 1950, "The Force Exerted by Surface Waves on Piles," J. Pet. Technol., **2**(05), pp. 149–154.

[20] Van den Boom, H., 1985, "Dynamic Behaviour of Mooring Lines," 4th International Conference on Behaviour of Offshore Structures, Delft, the Netherlands, July 1985.

[21] Jain, A., Goupee, A. J., Robertson, A. N., Kimball, R. W., Jonkman, J. M., and Swift, A. H., 2012, "Fast Code Verification of Scaling Laws for Deepcwind Floating Wind System," ISOPE International Ocean and Polar Engineering Conference, Rhodes, Greece, June 17–22.

[22] Orcina, 2023, L02 OC4 Semi-Sub. https://www.orcina.com/resources/examples/?key=l, Accessed July 31, 2023.

[23] Orcina, 2023, OrcaWave Documentation. https://www.orcina.com/webhelp/OrcaWave/Default.htm, Accessed November 19, 2023.

[24] Matha, D., Cruz, J., Masciola, M., Bachynski, E. E., Atcheson, M., Goupee, A. J., Gueydon, S. M., and Robertson, A. N., 2016, "Modelling of Floating Offshore Wind Technologies," *Floating Offshore Wind Energy: The Next Generation of Wind Energy*, Springer Cham, Switzerland, pp. 133–240.

[25] Newman, J. N., 1992, "Panel Methods in Marine Hydrodynamics," 11th Australasian Fluid Mechanics Conference, Hobart, Australia, December 1992.

[26] Lee, C.-H., Newman, J., and Zhu, X., 1996, "An Extended Boundary Integral Equation Method for the Removal of Irregular Frequency Effects," Int. J. Numer. Methods Fluids, **23**(7), pp. 637–660.

[27] Lee, C.H., 1988, *Numerical Methods for Boundary Integral Equations in Wave Body Interactions*, Massachusetts Institute of Technology, Cambridge, MA.

[28] Kvittem, M. I., Berthelsen, P. A., Eliassen, L., and Thys, M., 2018, "Calibration of Hydrodynamic Coefficients for a Semi-Submersible 10 MW Wind Turbine," International Conference on Offshore Mechanics and Arctic Engineering, Vol. 51319, American Society of Mechanical Engineers, p. V010T09A080.

[29] Liao, Y., and Wells, V., 2011, "Modal Parameter Identification Using the Log Decrement Method and Band-Pass Filters," J. Sound Vib., **330**(21), pp. 5014–5023.